Table 1: Patients who underwent VATS anatomical resection during this study period (n = 179)

Variables	No. of patients (%)
Age, median (years, range)	68 (26–87)
Sex	
Men	88 (49)
Women	91 (51)
Diagnosis	
Lung cancer	165 (92)
Metastatic lung tumour	6 (3)
Benign lung disease	8 (5)
Type of surgery	
Lobectomy	172 (96)
Right upper lobectomy	54
Right middle lobectomy	17
Right lower lobectomy	41
Right middle and lower lobectomy	2
Left upper lobectomy	37
Left lower lobectomy	21
Segmentectomy	7 (4)
Left S1+2–3	3
Right S3	1
Right S6	1
Left S4 + 5	1
Left S8–10	1
Preoperative 3D imaging	
Present	124 (69)
Absent	55 (31)

Table 2: Patients who underwent VATS anatomical resection with the preoperative 3D imaging (n = 124)

Variables	No. of patients (%)
Age, median (years, range)	68 (35–87)
Sex	
Men	60 (48)
Women	64 (52)
Diagnosis	
Lung cancer	115 (93)
Metastatic lung tumour	5 (4)
Benign lung disease	4 (3)
Type of surgery	
Lobectomy	119 (96)
Right upper lobectomy	38
Right middle lobectomy	13
Right lower lobectomy	27
Right middle and lower lobectomy	1
Left upper lobectomy	26
Left lower lobectomy	14
Segmentectomy	5 (4)
Left S1 + 2–3	2
Right S6	1
Left S4 + 5	1
Left S8–10	1
Conversion from VATS to thoracotomy	5 (4)
Operative time, mean (min, range)	230 (132–444)
Bleeding, mean (ml, range)	110 (0–1406)
Postoperative complications (Grade ≥ 2)	
Present	10 (8)
Arrhythmia	3
Prolonged air leakage	2
Chylothorax	1
Bacterial pneumonia	1
Bleeding	1
Empyema	1
Recurrent nerve paralysis	1
Absent	114 (92)
30-day mortality	0
90-day mortality	0

(96%) underwent lobectomy. This study involved 124 patients (69%) in whom 3D imaging was performed preoperatively and 55 patients (31%) in whom 3D imaging was not available because of contraindication to the use of contrast radiography (e.g., allergies to contrast medium, severe diabetes or bronchial asthma) or patient refusal against repeated imaging studies.

The characteristics and surgical outcomes of 124 patients undergoing 3D imaging are given in Table 2. There were 5 (4%) conversions from VATS to thoracotomy because of vessel bleedings. The frequency of patients presenting with complications with Grade 2 or above was 8% (n = 10), and there were no 30-day or 90-day operative mortalities.

According to intraoperative findings, PA branches were precisely identified on the basis of preoperative 3D-CT imaging (Table 3) in 97.8% (309 of 316) of vessels and 94.4% (117 of 124) of patients. There were 7 patients with undetected PA branches including 5 right upper lobectomies (RULs) and 2 left upper lobectomies (LULs). Undetected PA branches were the truncus arteriosus superior in 3 patients, the ascending artery in 2 patients, and the apical artery and lingular artery in 1 patient each. A representative image of an undetected ascending artery is shown in Fig. 1. The actual sizes of the 7 missed branches in the 7 patients were all less than 2 mm. The 3D image findings in PA branches were identical to operative findings in cases other than upper lobectomy. The number of patients with anomalous or uncommon PA branching patterns was 15 (12%). A summary of the 3D image findings in patients with anatomical variants of the PA is given in Supplementary material, Table S1. All anomalous or uncommon PA branches were accurately confirmed by 3D imaging. Of the 26 patients receiving LUL, 5 patients (19%) had anatomical variants of mediastinal lingular branches of the PA, which included the A4 + A5 type and either the A4 or A5 type. In addition, there were 5 patients with lingular PA arising from the basilar artery, 2 patients with 2 superior segmental arteries coming directly from the main PA, 2 patients with double ascending arteries, 1 patient without an ascending artery and 1 patient with triple middle lobe branches (Fig. 2). The 3D imaging showed 5 patients with anomalous PVs (Supplementary material, Table S2).

We evaluated the relationship between various clinical factors and the occurrence of postoperative complications (Table 4) or overall operative time (Table 5) in 165 patients with primary lung cancer. Sex (P = 0.002), pulmonary function test of forced expiratory volume in 1 s % (FEV1.0%; P = 0.011), and the presence or absence of respiratory comorbidities including chronic obstructive pulmonary disease, interstitial pneumonia, bronchial asthma etc. (P = 0.018) were found to be associated with the occurrence of complications. Conducting the preoperative 3D imaging tended to have associations, but the difference was not statistically significant (P = 0.054). On multivariate logistic regression analysis for these statistically or marginally significant factors, male gender was shown to be the only statistically significant independent predictor (risk ratio: 5.432, P = 0.013, Hosmer–Lemeshow χ^2 test = 0.89, P = 0.641), and 3D imaging also tended to be associated with the occurrence of complications (risk ratio: 2.852, P = 0.074).

There were significant associations between total operative time (dichotomized at mean operative time, 237 min) and conducting

Table 3: Identification rate of the 3D imaging in pulmonary artery branches according to type of surgery

Variables	No. of patients (%)	No. of PABs involved in resection		Identification rate (%)		Undetected PABs (no. of patients)
		3D images	Surgical findings	A per-vessel basis	A per-patient basis	
Overall	124 (100)	309	316	97.8	94.4	1 mm (1)/2 mm (6)
Type of surgery						
Right upper lobectomy	38 (31)	84	89	94.4	86.8	1 mm (1)/2 mm (4)
Right middle lobectomy	13 (10)	24	24	100	100	-
Right lower lobectomy	27 (22)	55	55	100	100	-
Right middle and lower lobectomy	1 (1)	2	2	100	100	-
Left upper lobectomy	26 (21)	99	101	98.0	92.3	2 mm (2)
Left lower lobectomy	14 (11)	33	33	100	100	-
Segmentectomy	5 (4)	12	12	100	100	-
Uncommon PAB pattern	15 (12)	50	50	100	100	-

PABs: pulmonary artery branches.

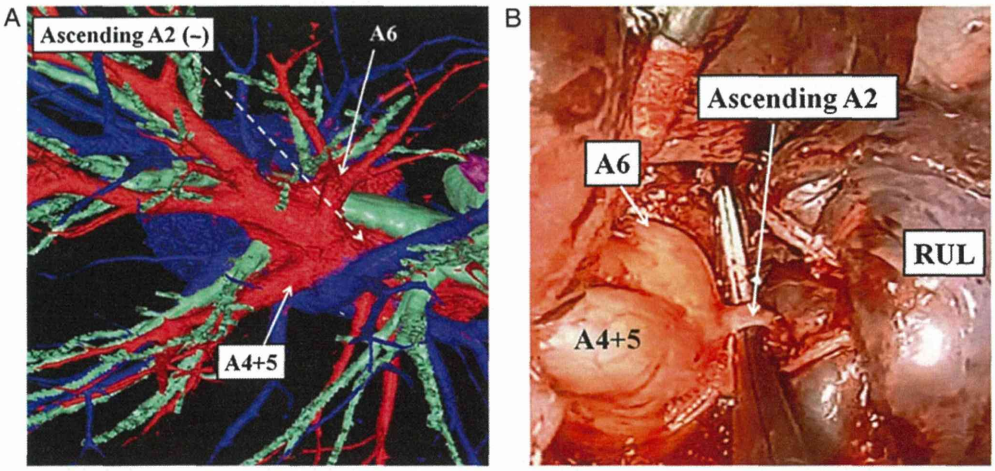

Figure 1: (**A**) A 3-dimensional computed tomographic image of the right pulmonary vessels. In this patient, a right upper lobectomy was performed. An ascending artery was not detected. (**B**) The intraoperative findings in this patient demonstrated the 2-mm ascending artery branches from the pulmonary artery.

the 3D imaging (risk ratio: 2.282, $P = 0.021$) and intraoperative blood loss (risk ratio: 1.005, $P = 0.005$) on univariate and multivariate analysis (Hosmer–Lemeshow χ^2 test = 5.92, $P = 0.656$).

DISCUSSION

We set out to identify the effectiveness of 3D-CT imaging for preoperative assessment of the branching patterns of pulmonary vessels and short-term surgical outcomes. A total of 97.8% of PA branches were precisely identified and all anomalous or uncommon PA and PV branching patterns were accurately confirmed by 3D imaging. In addition, patients undergoing preoperative 3D imaging tended to have lower incidences of postoperative complications and have significantly shorter operative time than those without the 3D simulations.

In reports in the literature concerning patients undergoing thoracoscopic and open surgery, 95–98% of PA branches were preoperatively identified using 3D-CT angiography, similar to our results [10–12]. Several authors also studied anomalous PA, PV or bronchial variations for surgery using 3D reconstruction [9, 12–15]. 3D simulation is considered to be useful in performing anatomical segmentectomy for small lung tumours for identifying the intersegmental veins as boundary lines of the pulmonary segments in order to determine the surgical margins using lateral 3D images and to identify the target segmental bronchi using vertical 3D images before segmentectomy [8, 16, 17]. These reports show that intraoperative visual guidance of the target pulmonary vessels and bronchi, and their relationship to one another as revealed by high-quality 3D images, could help thoracic surgeons perform safer anatomical lung resection and be prepared for more complicated operations.

In our clinical experience with using the Synapse Vincent software, there have been advantages of the 3D system that are based on volume-rendering techniques. First, a surgeon without expert knowledge concerning synthetic imaging can quickly and easily construct 3D images of each patient. The mean processing time required to construct a 3D angiographic image is approximately 5 min. The 3D imaging also allows us to freely rotate the objects and change the dimensions of images. The virtual 3D-CT can provide an overview of the 3D relationships of the pulmonary vessel pathways and the tracheobronchial tree. Thus, it is employed for preoperative simulations, which also help educate trainees about surgical anatomy. Secondly, unlike the currently

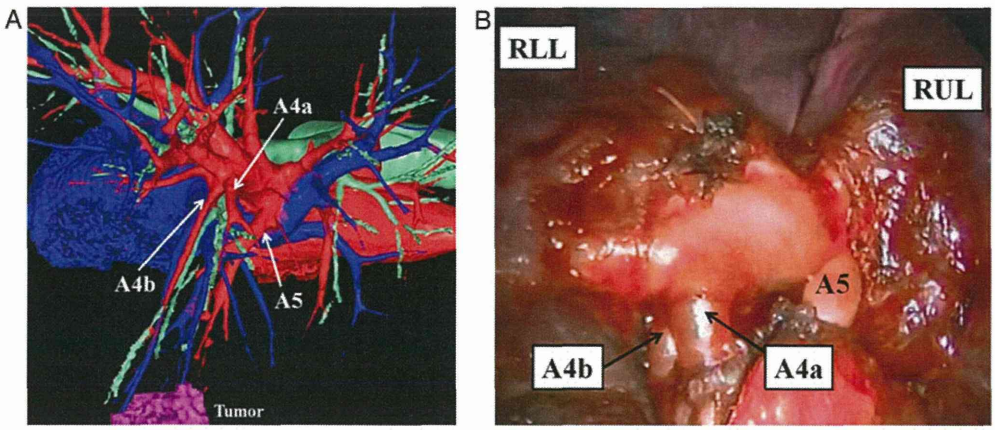

Figure 2: (**A**) The 3-dimensional computed tomographic image of the right pulmonary vessels showed that this patient had triple middle lobe pulmonary artery branches. (**B**) The intraoperative findings of this patient showed triple middle pulmonary artery branches corresponding to the 3-dimensional computed tomographic image.

Table 4: Association between clinical factors and the development of postoperative complications in patients who underwent VATS anatomical resection with primary lung cancer (n = 165)

Variables	Postoperative complications		Univariate analysis	Multivariate analysis		
	Present	Absent	*P*-value	RR	95% CI	*P*-value
Overall	18	147				
Sex						
Men	15	65		5.432		
Women	3	82	0.002	1	1.427–20.683	0.013
Age, median (years, range)	69 (27–87)		0.46			
Clinical staging						
IA	11	104				
IB	5	28				
IIA	1	7				
IIB	1	3				
IIIA	0	4				
IIIB	0	1	0.81			
Tumour location						
Right upper lobe	4	47				
Right middle lobe	2	14				
Right lower lobe	4	35				
Left upper lobe	6	34				
Left lower lobe	2	17	0.87			
Preoperative 3D imaging						
Present	9	106		1		
Absent	9	41	0.054	2.852	0.904–8.999	0.074
FEV1.0%, median (%, range)	74 (44–89)		0.011	0.962	0.891–1.039	0.861
Operative procedure						
Lobectomy	18	143				
Segmentectomy	0	4	0.48			
Conversion from VATS to thoracotomy						
Present	0	6				
Absent	18	141	0.38			
Intraoperative blood loss, mean (ml, range)	112 (0–1406)		0.89			
Operative time, mean (min, range)	237 (131–455)		0.65			
Respiratory comorbidity						
Present	8	29		1.153	0.233–5.716	
Absent	10	118	0.018	1		0.25
Cardiovascular comorbidity						
Present	1	10	0.51			
Absent	17	137				
Diabetes						
Present	0	7	0.34			
Absent	18	140				

RR: risk ratio; CI: confidence interval; FEV1.0: forced expiratory volume in 1 s.

Table 5: Association between clinical factors and operative time (<237 min vs ≥237 min) in patients who underwent VATS anatomical resection with primary lung cancer ($n = 165$)

Variables	Univariate analysis, *P*-value	Multivariate analysis		
		RR	95% CI	*P*-value
Operative time, mean (min, range)	237 (132–455)			
Sex	0.26			
Age	0.15			
Clinical staging: IA/IB/IIA/IIB/IIIA/IIIB	0.25			
Tumour laterality: right/left	0.77			
Preoperative 3D imaging: present/absent	0.019	2.282	1.131–4.604	0.021
Conversion from VATS to thoracotomy: present/absent	0.77			
FEV1.0%	0.31			
Intraoperative blood loss	0.001	1.005	1.001–1.009	0.005
Operative procedure: lobectomy/segmentectomy	0.21			
Respiratory comorbidity: present/absent	0.08			
Cardiovascular comorbidity: present/ absent	0.24			
Diabetes: present/absent	0.68			

RR: risk ratio; CI: confidence interval; FEV1.0: forced expiratory volume in 1 s.

available 3D-CT software programs, this system can show 3D images of the PA and the PV separately from the data of only one conventional CT scan. It can thereby reduce the radiation exposure dose. In contrast to the conventional method, we do not have to inject contrast media rapidly, and the infusion rate is sufficient at 1.5–2 ml/s. Consequently, we have not had any leakage accidents during contrast media infusion.

The disadvantages of 3D imaging include its potential deficiency in identifying bilateral upper lobe PA branches owing to the anatomically complex overlap of PA and PV branches. The ascending artery and truncus superior artery are often misidentified and confused with the apical segment vein or interlobar veins on 3D imaging. This might be due to the far more complicated ramification patterns of the PA in the upper lobe, particularly in the right upper lobe, than in the middle and lower lobes. However, we postulate that 3D imaging should be deemed acceptable because of the relatively low frequency of undetected PA branches.

The optimal strategy of managing postoperative complications of VATS anatomical resection is to prevent their occurrence. Perioperative complications and mortality with VATS lobectomy have been reported to occur at rates of ~5–32% and 0–7%, respectively [2, 18–20]. In the present study, postoperative complications in patients undergoing 3D imaging occurred in 8% with no mortality, and the risk of development of any complication in patients with 3D imaging was lower in comparison to those without 3D imaging. Notably, preoperative 3D simulation as well as intraoperative bleeding amount had significant association with total operative time. Possible reasons to explain these results are the assumptions that detailed surgical simulation and shared virtual lung anatomical information provided by 3D images between operating surgeons and a thoracoscopist might improve the safe and efficient performance of VATS, without causing vascular injuries due to unusual PA branching patterns, and thereby support a calm and efficient setting during lung resection.

The frequency of conversion from VATS lobectomy to open thoracotomy has been reported to range from 2% to as high as 23% [18, 19, 21, 22]. Although the most crucial concern with unexpected conversion to open thoracotomy are the possible increases in the risk of mortality and the development of complications, no postoperative complications arose in our 5 patients undergoing the 3D-CT (date not shown). Depending on the skill and ability to predict which patients are more likely to require conversion, the occurrence of serious complications can often be avoided. 3D information will be useful in training surgeons learning VATS procedures by shared real-time imaging with an experienced surgeon, influencing a surgeon's learning curve.

The limitations of this study are its retrospective nature and potential bias. Patient selection bias in conducting the preoperative 3D imaging may influence the result of short-term benefits in adverse events and operative time. To truly show the benefits of 3D software, a prospective randomized trial is needed.

In conclusion, this study demonstrated that preoperative simulations using 3D-CT angiography for the assessment of pulmonary vessel branching patterns appear to be beneficial for the safe and efficient performance of VATS anatomical resection and for further understanding of the surgical anatomy related to general thoracic surgery. Further advances in 3D-CT imaging technology will be useful in the development of not only VATS and open thoracotomy, but also robotic surgeries and cognitive and technical surgical education systems, without exposing patients to unnecessary risks.

SUPPLEMENTARY MATERIAL

Supplementary material is available at *EJCTS* online.

ACKNOWLEDGEMENTS

The authors are indebted to the medical editors of the Department of International Medical Communications of Tokyo Medical University for their editorial review of the English manuscript.

Funding

This study was supported by a Grant-in-Aid for Scientific Research, Japan Society for the Promotion of Science (24592104), and the Ministry of Education, Culture, Sports, Science and Technology, Japan.

Conflict of interest: The authors received fixed compensation for the described intellectual property without financial interest in its production, distribution or marketing.

REFERENCES

[1] Yim AP, Wan S, Lee TW, Arifi AA. VATS lobectomy reduces cytokine responses compared with conventional surgery. Ann Thorac Surg 2000;70:243–7.
[2] Whitson BA, Andrade RS, Boettcher A, Bardales R, Kratzke RA, Dahlberg PS *et al.* Video-assisted thoracoscopic surgery is more favorable than thoracotomy for resection of clinical stage I non-small cell lung cancer. Ann Thorac Surg 2007;83:1965–70.
[3] Port JL, Mirza FM, Lee PC, Paul S, Stiles BM, Altorki NK. Lobectomy in octogenarians with non-small cell lung cancer: ramifications of increasing life expectancy and the benefits of minimally invasive surgery. Ann Thorac Surg 2011;92:1951–7.
[4] Swanson SJ, Meyers BF, Gunnarsson CL, Moore M, Howington JA, Maddaus MA *et al.* Video-assisted thoracoscopic lobectomy is less costly and morbid than open lobectomy: a retrospective multiinstitutional database analysis. Ann Thorac Surg 2012;93:1027–32.
[5] Nakamura T, Koide M, Nakamura H, Toyoda F. The common trunk of the left pulmonary vein injured incidentally during lung cancer surgery. Ann Thorac Surg 2009;87:954–5.
[6] Akiba T, Marushima H, Kamiya N, Odaka M, Kinoshita S, Takeyama H *et al.* Thoracoscopic lobectomy for treating cancer in a patient with an unusual vein anomaly. Ann Thorac Cardiovasc Surg2011;17:501–3.
[7] Ikeda N, Yoshimura A, Hagiwara M, Akata S, Saji H. Three dimensional computed tomography lung modeling is useful in simulation and navigation of lung cancer surgery. Ann Thorac Cardiovasc Surg 2013;19:1–5.
[8] Saji H, Inoue T, Kato Y, Shimada Y, Hagiwara M, Kudo Y *et al.* Virtual segmentectomy based on high-quality three-dimensional lung modelling from computed tomography images. Interact CardioVasc Thorac Surg 2013;17:227–32.
[9] Akiba T, Marushima H, Harada J, Kobayashi S, Morikawa T. Anomalous pulmonary vein detected using three-dimensional computed tomography in a patient with lung cancer undergoing thoracoscopic lobectomy. Gen Thorac Cardiovasc Surg 2008;56:413–6.
[10] Fukuhara K, Akashi A, Nakane S, Tomita E. Preoperative assessment of the pulmonary artery by three-dimensional computed tomography before video-assisted thoracic surgery lobectomy. Eur J Cardiothorac Surg 2008; 34:875–7.
[11] Watanabe S, Arai K, Watanabe T, Koda W, Urayama H. Use of three-dimensional computed tomographic angiography of pulmonary vessels for lung resections. Ann Thorac Surg 2003;75:388–92; discussion 92.
[12] Akiba T, Marushima H, Morikawa T. Confirmation of a variant lingular vein anatomy during thoracoscopic surgery. Ann Thorac Cardiovasc Surg 2010; 16:351–3.
[13] Ishikawa Y, Iwano S, Usami N, Yokoi K. An anomalous segmental vein of the left upper lobe of the lung: preoperative identification by three-dimensional computed tomography pulmonary angiography. Interact CardioVasc Thorac Surg 2012;15:512–3.
[14] Akiba T, Morikawa T, Marushima H, Nakada T, Inagaki T, Ohki T. Computed Tomography Guided Thoracoscopic Segmentectomy for Lung Cancer with Variant Bronchus. Ann Thorac Cardiovasc Surg 2014;20: 407–9.
[15] Nakashima S, Watanabe A, Ogura K, Higami T. Advantages of preoperative three-dimensional contrast-enhanced computed tomography for anomalous pulmonary artery in video-assisted thoracoscopic segmentectomy. Eur J Cardiothorac Surg 2010;38:388.
[16] Oizumi H, Kanauchi N, Kato H, Endoh M, Suzuki J, Fukaya K *et al.* Anatomic thoracoscopic pulmonary segmentectomy under 3-dimensional multidetector computed tomography simulation: a report of 52 consecutive cases. J Thorac Cardiovasc Surg 2011;141:678–82.
[17] Shimizu K, Nakano T, Kamiyoshihara M, Takeyoshi I. Segmentectomy guided by three-dimensional computed tomography angiography and bronchography. Interact CardioVasc Thorac Surg 2012;15:194–6.
[18] Walker WS, Codispoti M, Soon SY, Stamenkovic S, Carnochan F, Pugh G. Long-term outcomes following VATS lobectomy for non-small cell bronchogenic carcinoma. Eur J Cardiothorac Surg 2003;23:397–402.
[19] McKenna RJ Jr, Houck W, Fuller CB. Video-assisted thoracic surgery lobectomy: experience with 1100 cases. Ann Thorac Surg 2006;81:421–5; discussion 25–6.
[20] Lewis RJ, Caccavale RJ, Bocage JP, Widmann MD. Video-assisted thoracic surgical non-rib spreading simultaneously stapled lobectomy: a more patient-friendly oncologic resection. Chest 1999;116:1119–24.
[21] Hennon M, Sahai RK, Yendamuri S, Tan W, Demmy TL, Nwogu C. Safety of thoracoscopic lobectomy in locally advanced lung cancer. Ann Surg Oncol 2011;18:3732–6.
[22] Roviaro G, Varoli F, Vergani C, Maciocco M, Nucca O, Pagano C. Video-assisted thoracoscopic major pulmonary resections: technical aspects, personal series of 259 patients, and review of the literature. Surg Endosc 2004; 18:1551–8.

Case Study

ASIAN CARDIOVASCULAR & THORACIC ANNALS

Asian Cardiovascular & Thoracic Annals
0(0) 1–3

DOI: 10.1177/0218492314547543
aan.sagepub.com
SAGE

High-quality 3-dimensional imaging for patients with anomalous pulmonary veins

Kentaro Fukuta, Yoshihisa Shimada, Masaru Hagiwara, Naohiro Kajiwara, Tatsuo Ohira and Norihiko Ikeda

Abstract

The branching pattern of pulmonary veins exhibits many variations. Here we describe 2 patients with lung malignancies who were found to have pulmonary vein anomalies. We performed video-assisted thoracoscopic lobectomies based on preoperative simulations by 3-dimensional computed tomography. Using 3-dimensional computed tomography, a surgeon can easily construct digital images of the patient's pulmonary vessels within a few minutes. Simulation using 3-dimensional computed tomography imaging is useful for further understanding of the surgical anatomy.

Keywords

Lung neoplasms, Pneumonectomy, Pulmonary veins, Thoracic surgery, Video-assisted, Tomography, X-ray computed

Introduction

Video-assisted thoracic surgery (VATS) for anatomical lung resection requires precise knowledge of the pulmonary vessels and bronchi because of the narrow operative field and reduced tactile sensations. Preoperative simulations of the surgical anatomy are of considerable value because anatomic anomalies of pulmonary vessels can cause serious intraoperative problems such as bleeding.[1,2] Preoperatively, we have used a high-quality three-dimensional computed tomography (3D-CT) image analysis system (Synapse Vincent, Fuji Film Co., Ltd., Tokyo, Japan) for constructing virtual-reality 3D pulmonary anatomy since 2011.[3] Here we report 2 cases of anomalous pulmonary vein anatomy in which we performed VATS lobectomy based on preoperative simulations by 3D-CT.

Case 1

An 83-year-old woman had an abnormal shadow in the right lung on a routine medical check-up. An enhanced CT scan demonstrated a 1.9-cm nodule in the right lower lobe and the superior segment of the right lower lobe vein (V6) ostium, separate from the inferior pulmonary vein and each other (Figure 1A). The 3D-CT image clearly showed that the V6 directly drained into the left atrium just below the superior pulmonary vein (Figure 1B). Initially, we performed thoracoscopic partial resection and intraoperative rapid diagnosis indicated adenocarcinoma. Subsequently, we performed a VATS right lower lobectomy with lymph node dissection through 4 access ports. The V6 independently drained into the left atrium (Figure 1C). Figure 1D shows a schema of this anomalous V6. This independent V6 and the inferior pulmonary vein were therefore carefully ligated with a surgical stapler. The postoperative course was uneventful and the pathological diagnosis was stage IA lung adenocarcinoma.

Case 2

A 70-year-old woman was referred to our institution with an abnormality in the right lung field on a chest radiograph. An enhanced CT scan showed a lesion measuring 1.5 cm × 1.4 cm in the right S2 area and a right upper lobe vein posterior to the bronchus intermedius (Figure 2A). A review of the patient's 3D-CT image clearly showed that the right upper lobe vein was directly connected to the inferior pulmonary vein (Figure 2B). VATS right upper lobectomy with lymph

First Department of Surgery, Tokyo Medical University Hospital, Tokyo, Japan

Corresponding author:
Yoshihisa Shimada, First Department of Surgery, Tokyo Medical University Hospital, 6-7-1 Nishishinjuku, Shinjuku-ku, Tokyo 160-0023, Japan.
Email: zenkyu@za3.so-net.ne.jp

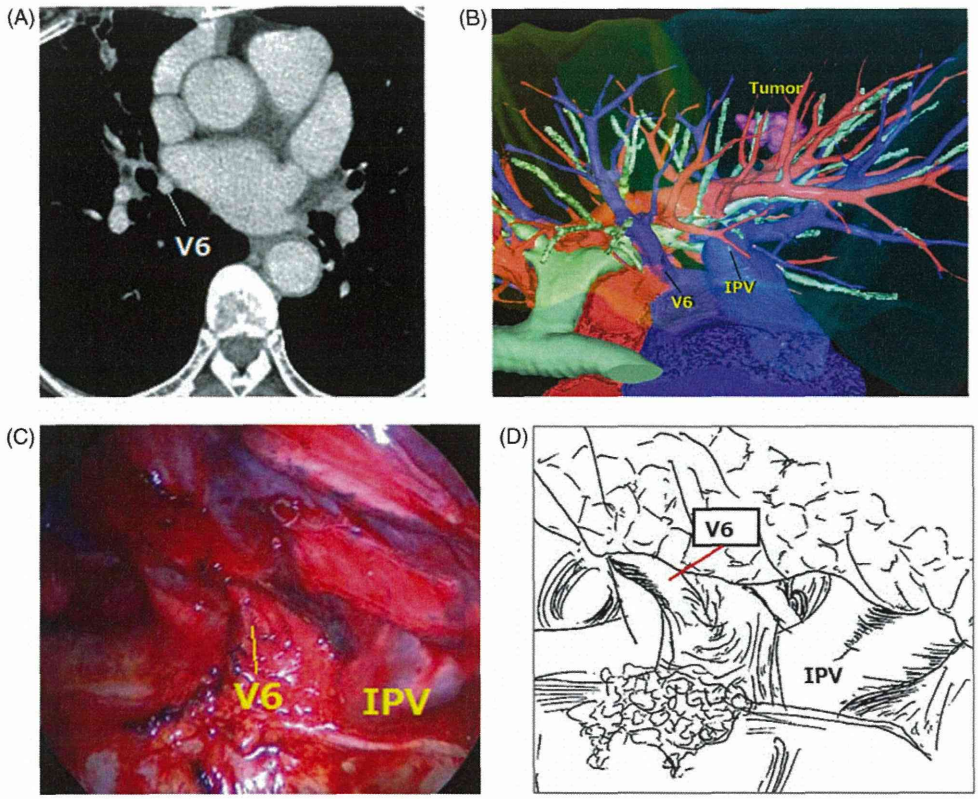

Figure 1. Case 1. (A) Enhanced computed tomography image showing the superior segment of the right lower lobe vein (V6) ostium separate from the inferior pulmonary vein (IPV; white arrow). (B) Virtual 3-dimensional computed tomography image showing that the V6 directly draining into the left atrium. (C) Intraoperative image demonstrating that the V6 drained independently into the left atrium. (D) Schema of this anomalous V6.

node dissection was performed through 4 access ports. We separated the abnormal right upper lobe vein from the bronchus intermedius and surrounding lung tissue (Figure 2C). Figure 2D shows a schema of the anomalous right upper lobe vein. After the abnormal vein was divided between double ligatures, the posterior aspect of the major fissure was carefully divided. The patient's postoperative course was uneventful, and the histological diagnosis was a metastatic lung tumor from breast cancer treated 10 years previously.

Discussion

Preoperative identification of anomalous pulmonary vessels is thought to be important for avoiding injury to vessels and for further understanding of pulmonary anatomy.[1–5] Therefore, preoperative simulation of the surgical anatomy using imaging modalities is desirable. There are various advantages of this 3D-CT software that is based on volume-rendering techniques. First, a surgeon without expert knowledge concerning synthetic imaging can quickly construct each patient's 3D images. After the digital images from enhanced CT are transferred to the 3D system by compact disk read-only memory, the system displays 3D images automatically within a few minutes. The software also allows us to freely rotate the objects and to change their dimensions. Intraoperative visualization guidance of the target vessels and bronchi and their relationship to one another should help surgeons perform lung resections with fewer complications, and be prepared for complicated operations such as multi-segmentectomies. Furthermore, unlike the currently available 3D-CT software programs, this system can obtain 3D images of the pulmonary artery and the veins separately, compared to only one image obtained from a conventional CT scan. Therefore, it can reduce the radiation exposure dose.

As demonstrated by the 2 cases presented here, this 3D-CT imaging technique is useful for identifying anomalous pulmonary vein connections. In case 2, it might have been difficult to identify the anomalous vein using conventional CT. Asai and colleagues[6] reported that the frequency of the right upper lobe vein being positioned posterior to the bronchus intermedius, as in case 2, is 5.7%. Cronin and colleagues[7] reported that 2.5% of patients had an accessory pulmonary vein at the superior segment of the right lower lobe, similar to case 1. We consider preoperative simulations using 3D-CT to be useful for the safe performance of VATS lobectomy and for further understanding

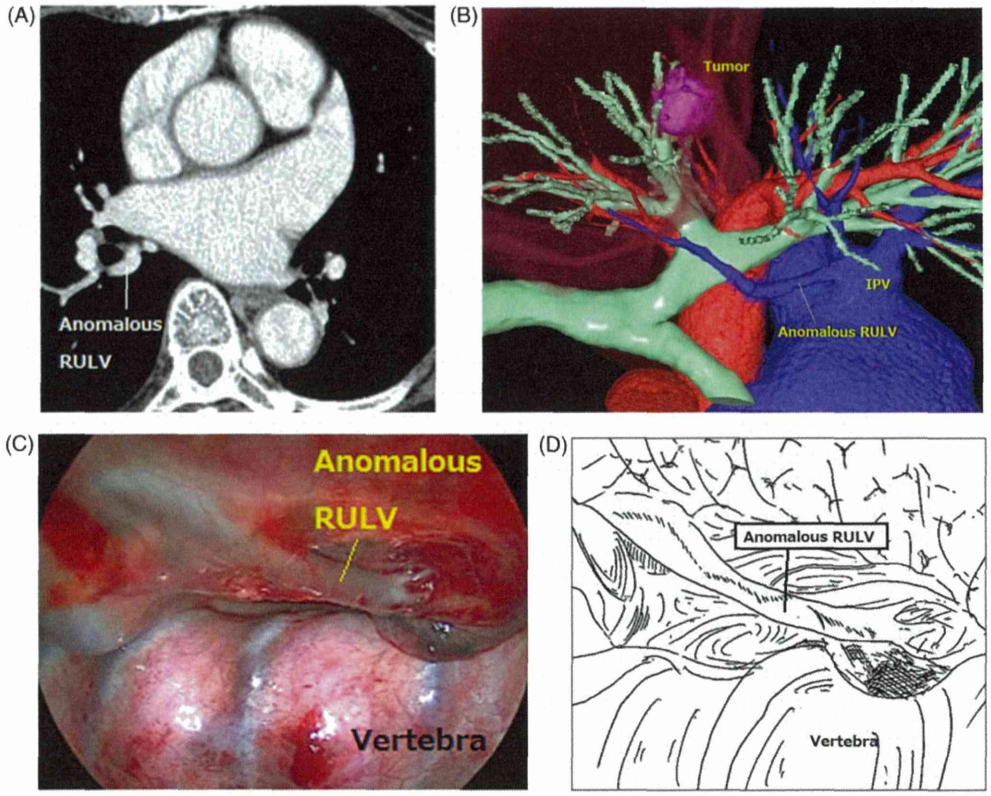

Figure 2. Case 2. (A) Enhanced computed tomography image showing a right upper lobe vein (RULV) posterior to the bronchus intermedius (white arrow). (B) Three-dimensional computed tomography image showing the right upper lobe vein directly connected to the inferior pulmonary vein (IVP) positioned posterior to the bronchus intermedius. (C) Intraoperative findings showing the anomalous right upper lobe vein corresponding to the 3-dimensional computed tomography image. (D) Schema of the anomalous right upper lobe vein.

of the surgical anatomy. Further advances in 3D-CT imaging technology should lead to significant developments not only in VATS and thoracotomy, but also in robotic surgeries and surgical education systems.

Acknowledgement

The authors are indebted to the medical editors of the Department of International Medical Communications of Tokyo Medical University for their editorial review of the English manuscript.

Funding

This research received no specific grant from any funding agency in the public, commercial, or not-for-profit sectors.

Conflict of interest statement

None declared.

References

1. Nakamura T, Koide M, Nakamura H and Toyoda F. The common trunk of the left pulmonary vein injured incidentally during lung cancer surgery. *Ann Thorac Surg* 2009; 87: 954–955.
2. Endo S, Tsubochi H, Nakano T and Sohara Y. A dangerous venous variation in thoracoscopic right lower lobectomy. *Ann Thorac Surg* 2009; 87: e9–e10.
3. Ikeda N, Yoshimura A, Hagiwara M, Akata S and Saji H. Three-dimensional computed tomography lung modeling is useful in simulation and navigation of lung cancer surgery. *Ann Thorac Cardiovasc Surg* 2013; 19: 1–5.
4. Akiba T, Marushima H, Kamiya N, et al. Thoracoscopic lobectomy for treating cancer in a patient with an unusual vein anomaly. *Ann Thorac Cardiovasc Surg* 2011; 17: 501–503.
5. Greene R and Miller SW. Cross-sectional imaging of silent pulmonary venous anomalies. *Radiology* 1986; 159: 279–281.
6. Asai K, Urabe N, Yajima K, Suzuki K and Kazui T. Right upper lobe venous drainage posterior to the bronchus intermedius: preoperative identification by computed tomography. *Ann Thorac Surg* 2005; 79: 1866–1871.
7. Cronin P, Kelly AM, Desjardins B, et al. Normative analysis of pulmonary vein drainage patterns on multidetector CT with measurements of pulmonary vein ostial diameter and distance to first bifurcation. *Acad Radiol* 2007; 14: 178–188.

Cell Research (2014) 24:994-1008.

www.nature.com/cr

ORIGINAL ARTICLE

A Smad3 and TTF-1/NKX2-1 complex regulates Smad4-independent gene expression

Kazunobu Isogaya[1], Daizo Koinuma[1], Shuichi Tsutsumi[2], Roy-Akira Saito[1,3], Keiji Miyazawa[1,4], Hiroyuki Aburatani[2], Kohei Miyazono[1]

[1]Department of Molecular Pathology, Graduate School of Medicine, The University of Tokyo, Bunkyo-ku, Tokyo 113-0033, Japan; [2]Genome Science Division, Research Center for Advanced Science and Technology (RCAST), The University of Tokyo, Meguro-ku 153-8904, Japan; [3]Department of Respiratory Medicine, Graduate School of Medicine, The University of Tokyo, Bunkyo-ku, Tokyo 113-0033, Japan; [4]Department of Biochemistry, Interdisciplinary Graduate School of Medicine and Engineering, University of Yamanashi, 1110 Shimokato, Chuo, Yamanashi 409-3898, Japan

Thyroid transcription factor-1 (TTF-1, also known as NKX2-1) is a tissue-specific transcription factor in lung epithelial cells. Although TTF-1 inhibits the epithelial-to-mesenchymal transition induced by transforming growth factor-β (TGF-β) in lung adenocarcinoma cells, the mechanism through which TTF-1 inhibits the functions of TGF-β is unknown. Here we show that TTF-1 disrupts the nuclear Smad3-Smad4 complex without affecting the nuclear localization of phospho-Smad3. Genome-wide analysis by chromatin immunoprecipitation followed by sequencing revealed that TTF-1 colocalizes with Smad3 on chromatin and alters Smad3-binding patterns throughout the genome, while TTF-1 generally inhibits Smad4 binding to chromatin. Moreover, Smad3 binds to chromatin together with TTF-1, but not with Smad4, at some Smad3-binding regions when TGF-β signaling is absent, and knockdown of Smad4 expression does not attenuate Smad3 binding in these regions. Thus, TTF-1 may compete with Smad4 for interaction with Smad3, and in the presence of TTF-1, Smad3 regulates the transcription of certain genes independently of Smad4. These findings provide a new model of regulation of TGF-β-Smad signaling by TTF-1.

Keywords: ChIP-seq; NKX2-1; Smad3; Smad4; TTF-1; TGF-β

Cell Research (2014) **24**:994-1008. doi:10.1038/cr.2014.97; published online 25 July 2014

Introduction

Thyroid transcription factor-1 (TTF-1), also known as NKX2-1, is a tissue-specific homeodomain transcription factor expressed only in lung, bronchi, thyroid grand and forebrain. In the lung, TTF-1 is strongly expressed in type II alveolar cells and Clara cells, and regulates the expression of genes that encode surfactant proteins, such as *SFTPB* (encoding surfactant protein B). TTF-1 is thus thought to be the master regulator of lung epithelial differentiation [1].

TTF-1 is expressed in 75%-80% of lung adenocarcinoma patients [2, 3]. Among patients with lung adenocarcinoma, those with TTF-1-positive cancer exhibit better prognosis than those with TTF1-negative cancer [4-6]. Using a transgenic lung cancer mouse model, deletion of *TTF-1* has been shown to promote invasion and metastasis of lung adenocarcinoma, in part due to the role of TTF-1 in HMGA2 expression [7]. TTF-1 was also shown to reduce cell motility and metastasis through induction of *MYBPH* expression [8]. These findings strongly suggest that TTF-1 functions as a tumor suppressor in lung adenocarcinoma. In contrast, genomics analyses revealed that human *TTF1/NKX2-1* gene was amplified in 10%-15% of lung adenocarcinomas; it is therefore called a lineage-survival oncogene [9-12]. TTF-1 has been shown to exhibit a pro-survival effect by inducing ROR1 expression, which enhances AKT signaling through the EGF-ErbB3-PI3 kinase axis [13]. It has also recently been reported that amplified TTF-1 and FOXA1 cooperatively regulate expression of the *LMO3* oncogene, which me-

Correspondence: Kohei Miyazono[a], Daizo Koinuma[b]
[a,b]Tel: +81-3-5841-3345; Fax: +81-3-5841-3354
[a]E-mail: miyazono@m.u-tokyo.ac.jp
[b]E-mail: koinuma@m.u-tokyo.ac.jp
Received 21 November 2013; revised 6 April 2014; accepted 4 May 2014; published online 25 July 2014

diates cell survival downstream of TTF-1 [14]. Although the precise mechanism(s) of favorable prognosis brought by TTF-1 remains unknown, it is possible that TTF-1 interacts with other transcription factors and alters their signaling activities.

Transforming growth factor-β (TGF-β) is a multifunctional cytokine with bidirectional roles in cancer progression [15, 16]. TGF-β binds to type II and type I receptors, resulting in phosphorylation of the receptor-regulated Smads (R-Smads): Smad2 and Smad3. R-Smads form hetero-oligomeric complexes with Smad4, and translocate into the nucleus [15, 16], where they regulate the transcription of target genes through interaction with other transcription factors. Smad3 and Smad4 bind directly to chromatin through their N-terminal MH1 domains; Smad2 does not bind directly to chromatin because of an insert sequence that is present in its MH1 domain [17, 18]. Several groups have reported genome-wide analyses of the binding patterns of TGF-β receptor-regulated Smads in various cancer cell lines and embryonic stem cell-derived cells [19-25]. These results reveal varied Smad-binding profiles in different cell types, indicating that "cell-specific context" is important for the response to TGF-β signaling.

Smad3 reportedly regulates the transcriptional activity of TTF-1 [26, 27]. We previously reported that TTF-1 inhibits TGF-β-induced epithelial-to-mesenchymal transition (EMT) in lung adenocarcinoma cells [28]. Conversely, TGF-β decreased endogenous expression of TTF-1 [28]. Thus, functional links between TTF-1 and TGF-β signaling appear to be important for the progression of lung adenocarcinoma. Genome-wide analyses of TTF-1 binding have recently been reported [14, 29]; however, how TTF-1 regulates TGF-β-Smad signaling remains to be elucidated. Here, we identified and compared Smad3-, Smad4- and TTF-1-binding sites in the H441 lung adenocarcinoma cell line to understand the mechanism by which TTF-1 inhibits TGF-β signaling. Our data suggest that TTF-1 regulates TGF-β-Smad signaling by competing with Smad4, and that Smad3 acts together with TTF-1 to regulate expression of certain genes, e.g., *LMO3*, in a Smad4-independent manner. TTF-1 may therefore contribute to context-dependent regulation of TGF-β and Smad3 signaling in lung epithelial cells and lung adenocarcinoma cells.

Results

TTF-1 disrupts the Smad3-Smad4 complex

First, we examined whether TTF-1 affects the complex formation of Smad3 with Smad4, as well as the phosphorylation and nuclear translocation of Smad3. TTF-1 was exogenously expressed in A549 cells, which lack the expression of endogenous TTF-1, with an adenoviral vector AdTTF-1. Co-immunoprecipitation assay demonstrated that TTF-1 bound to Smad3 with or without TGF-β stimulation, and formation of the Smad3 and Smad4 (Smad3-Smad4) complex induced by TGF-β was strongly inhibited by TTF-1 overexpression (Figure 1A). Next, we fractionated the nucleus and cytoplasm of A549 cells infected with AdTTF-1, and detected phosphorylated Smad3 (pSmad3) by immunoblotting. pSmad3 was detected in the nucleus upon TGF-β stimulation, while TTF-1 was located mainly in the nucleus in the presence or absence of TGF-β stimulation (Figure 1B). TTF-1 overexpression did not suppress either phosphorylation of Smad3 or nuclear translocation of Smad3 and Smad4.

We also confirmed the localization of Smad3 and Smad2 using an *in situ* proximity ligation assay (*in situ* PLA). In agreement with the findings of the subcellular fractionation experiments (Figure 1B), forced expression of TTF-1 did not affect TGF-β-induced nuclear translocation of Smad3 and Smad2 (Supplementary information, Figure S1A). By using anti-TTF-1 and anti-Smad3 antibodies, we found that TTF-1 was located in the vicinity of Smad3 in the nucleus with or without TGF-β stimulation (Supplementary information, Figure S1B).

Next, we assessed formation of the Smad3-Smad4 complex by *in situ* PLA (Figure 1C). The Smad3-Smad4 complex was observed in both the nucleus and the cytoplasm in A549 cells infected with a control adenovirus (AdLacZ), and most of the nuclear Smad3-Smad4 complex disappeared in the presence of TTF-1. The nuclear complex containing Smad2 and Smad4 was also decreased by TTF-1 overexpression (data not shown). We then performed *in situ* PLA assays using H441 human lung adenocarcinoma cells, which endogenously express TTF-1 [28]. Knockdown of TTF-1 by siRNA treatment (Supplementary information, Figure S4A) increased the number of nuclear Smad3-Smad4 complexes in H441 cells (Figure 1D), suggesting that TTF-1 disrupts the Smad3-Smad4 complex in the nucleus.

TTF-1 inhibits Smad3 binding to chromatin

TTF-1 has been reported to inhibit certain TGF-β-Smad3 signaling pathways [28]; therefore, it is possible that Smad3 is present in the nucleus but fails to bind to target genomic regions in the presence of TTF-1. Thus, we performed chromatin immunoprecipitation (ChIP)-quantitative PCR (qPCR) analysis using a Smad3-specific antibody. Exogenous expression of TTF-1 strongly inhibited the binding of Smad3 to the *plasminogen activator inhibitor-1* (*PAI-1*, also known as *SERPINE1*) and *SMAD7* promoters (Figure 1E). Next, we

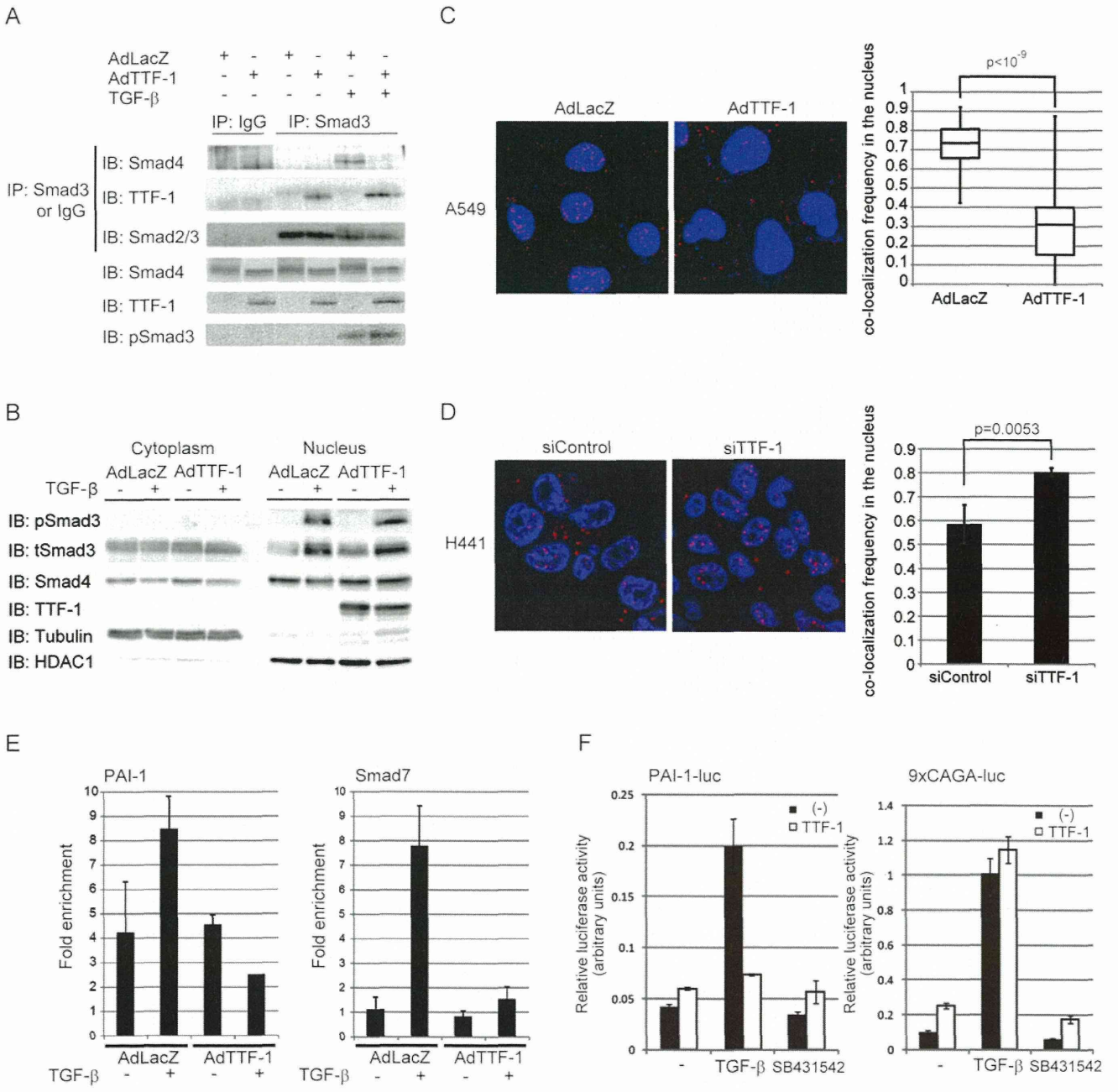

Figure 1 TTF-1 interacts with Smad3 independently of TGF-β and inhibits Smad3-Smad4-induced transcription of target genes. **(A)** A549 cells were infected with the adenoviral TTF-1 expression vector (AdTTF-1) or control adenovirus (AdLacZ) as indicated. At 24 h post-infection, cells were treated with TGF-β for 1.5 h. Cell lysates were immunoprecipitated (IP) with anti-Smad3 antibody or control mouse IgG, and Smad3-bound TTF-1 and Smad4 were detected by immunoblotting (IB). **(B)** A549 cells were infected with adenoviral vectors as in **A**. Nucleic and cytoplasmic fractions of the cells were obtained 2 h after TGF-β stimulation, and the levels of phosphorylated Smad3 (pSmad3), total Smad3 (tSmad3) and Smad4 were detected by IB. **(C, D)** A549 cells infected with the indicated adenoviral vectors (AdLacZ or AdTTF-1) **(C)** and H441 cells transfected with control siRNA (siControl) or TTF-1 siRNA (siTTF-1) **(D)** were treated with TGF-β for 1.5 h, and the Smad3-Smad4 complex was detected using anti-Smad3 and anti-Smad4 antibodies. PLA signals (red) detected in the nuclei (blue) of A549 cells infected with AdLacZ or AdTTF-1 or H441 cells treated with siControl or siTTF-1 were counted (right panels). **(E)** A549 cells were infected with adenoviral TTF-1 or LacZ expression vectors and treated with TGF-β for 1.5 h. Then, a ChIP assay using Smad3-specific antibody was performed to analyze the binding of Smad3 to the *PAI-1* and *SMAD7* promoter regions. **(F)** A549 cells were transfected with the TTF-1-expression vector or control vector and treated with TGF-β for 12 h or SB431542 for 12 h. Luciferase reporter assays using PAI-1-luc containing *PAI-1* natural promoter or 9× CAGA-luc containing tandemly repeated SBEs were performed.

examined the effects of TTF-1 on TGF-β-induced transcription using a luciferase reporter containing the *PAI-1* promoter (PAI-1-luc) and a reporter containing tandemly repeated Smad-binding elements (SBEs; 9× CAGA-luc). TTF-1 overexpression inhibited the promoter activity of PAI-1-luc induced by TGF-β, but did not affect that of 9× CAGA-luc (Figure 1F). However, treatment with the TGF-β type I receptor inhibitor SB431542 effectively reduced TGF-β-induced activation of both reporters (Figure 1F). These findings suggest that certain *cis*-regulatory element(s) other than the canonical SBE might be required for TTF-1 to inhibit Smad-induced transcription.

Genome-wide identification of Smad3-, Smad4- and TTF-1-binding regions in H441 cells

Next, we performed ChIP-seq analyses using H441 cells transfected with siRNA for TTF-1 (siTTF-1) or control siRNA (siControl), and stimulated the cells with TGF-β. Using a false discovery ratio (FDR) cut-off of 0.01, we have identified 8 941 and 14 145 Smad3-binding regions from the ChIP-seq data of TGF-β-treated H441 cells transfected with control and TTF-1 siRNAs, respectively. ChIP-seq data from TGF-β-stimulated H441 cells with and without TTF-1 siRNA yielded 1 605 and 1 Smad4-binding peaks, respectively, with a FDR cutoff of 0.1; the same sample set also yielded 21 292 and 31 083 TTF-1-binding peaks with and without TGF-β stimulation, respectively, with a FDR cutoff of 0.01 (Supplementary information, Tables S1-S6).

There were several significant Smad3- and Smad4-binding peaks in the promoter region of *PAI-1* gene, as previously reported [25] (see Figure 2D). The enrichment of Smad3 in the *PAI-1* promoter region was validated by ChIP-qPCR (Supplementary information, Figure S2). There were also significant TTF-1-binding peaks in the promoter region of *SFTPB* gene [14] (Supplementary information, Figure S3A and S3B). We performed *de novo* motif prediction in the TTF-1 ChIP-seq data using the CisGenome Gibbs motif sampler. One of the obtained motifs (Supplementary information, Figure S3C) was very similar to the TTF-1-binding motif recently reported by others [14], indicating that the ChIP-seq analysis appeared to successfully recognize binding regions of TTF-1.

Binding of Smad3 to chromatin at the Smad3-only regions is mainly affected by TTF-1

We compared the identified Smad3-, Smad4- and TTF-1-binding peaks obtained by the ChIP-seq analyses of H441 cells. Approximately 80% (7 201/8 941) of the Smad3-binding peaks in H441 cells treated with siControl were also observed in cells treated with siTTF-1 (Figure 2A-i). When transfected with TTF-1 siRNA, approximately 75% (1 281/1 605) of the Smad4-binding peaks were common to the Smad3-binding peaks (Figure 2A-ii). It should be noted that the number of binding sites of each transcription factor depends on the efficiency of antibodies used for ChIP analysis, and that the ChIP efficiency of the anti-Smad4 antibody was much lower than that of the anti-Smad3 antibody. More than 85% (7 839/8 941) of the Smad3-binding peaks were common to the TTF-1-binding peaks (Figure 2B-i). Knockdown of TTF-1 increased the number of Smad3-binding peaks, but most of the new peaks were not common to TTF-1-binding peaks (Figure 2B-ii). About one-half (797/1 605) of the Smad4-binding peaks in siTTF-1-transfected cells were common to TTF-1-binding peaks (Figure 2B-iii).

To analyze these data quantitatively, we obtained a read count of each Smad3-binding peak from the ChIP-seq data of Smad3 in H441 cells treated with siTTF-1 and siControl. We then calculated the siControl/siTTF-1 ratio of the read counts at each binding peak. If this ratio is high, then TTF-1 does not tend to inhibit Smad3 binding in the respective region. If the ratio is low, the binding strength of Smad3 in the respective region is likely to be attenuated by the presence of TTF-1. We arranged the Smad3-binding peaks with respect to these ratios, chose the top 2 000 and bottom 2 011 peaks and examined whether there were any TTF-1-binding region(s) within 200 bps of the peak summit. Interestingly, more than 80% of the top 2 000 binding peaks have TTF-1-binding regions within 200 bps of their binding summits, while TTF-1 binds to only 8% of the bottom 2 011 peaks (Figure 2C). Therefore, Smad3 colocalizes with TTF-1 on chromatin in the presence of TTF-1, and the inhibitory effect of TTF-1 on Smad3 does not appear to be induced by competition in chromatin binding.

Analysis of the ChIP-seq data revealed two types of Smad3-binding regions, i.e., Smad3-TTF-1 common regions and Smad3-only regions, even around a single target gene locus. For example, there are seven Smad3-binding peaks around the *PAI-1* gene; two of them are Smad3-TTF-1 common regions (Figure 2D, peaks f and g) and five are Smad3-only regions (Figure 2D, peaks a-e). We performed sequential anti-Smad3 and anti-Smad4 ChIP-qPCR at the peak e in Figure 2D. We found that Smad3 and Smad4 were colocalized at this peak, and that the binding strength was increased when TTF-1 was knocked down (Figure 2E). Next, we used scatter plotting to compare the changes in read counts of Smad3-TTF-1 common regions (Figure 2F, upper panel) or Smad3-only regions (Figure 2F, lower panel) between siControl- and siTTF-1-transfected cells. The read counts in most of the Smad3-TTF-1 common regions did not

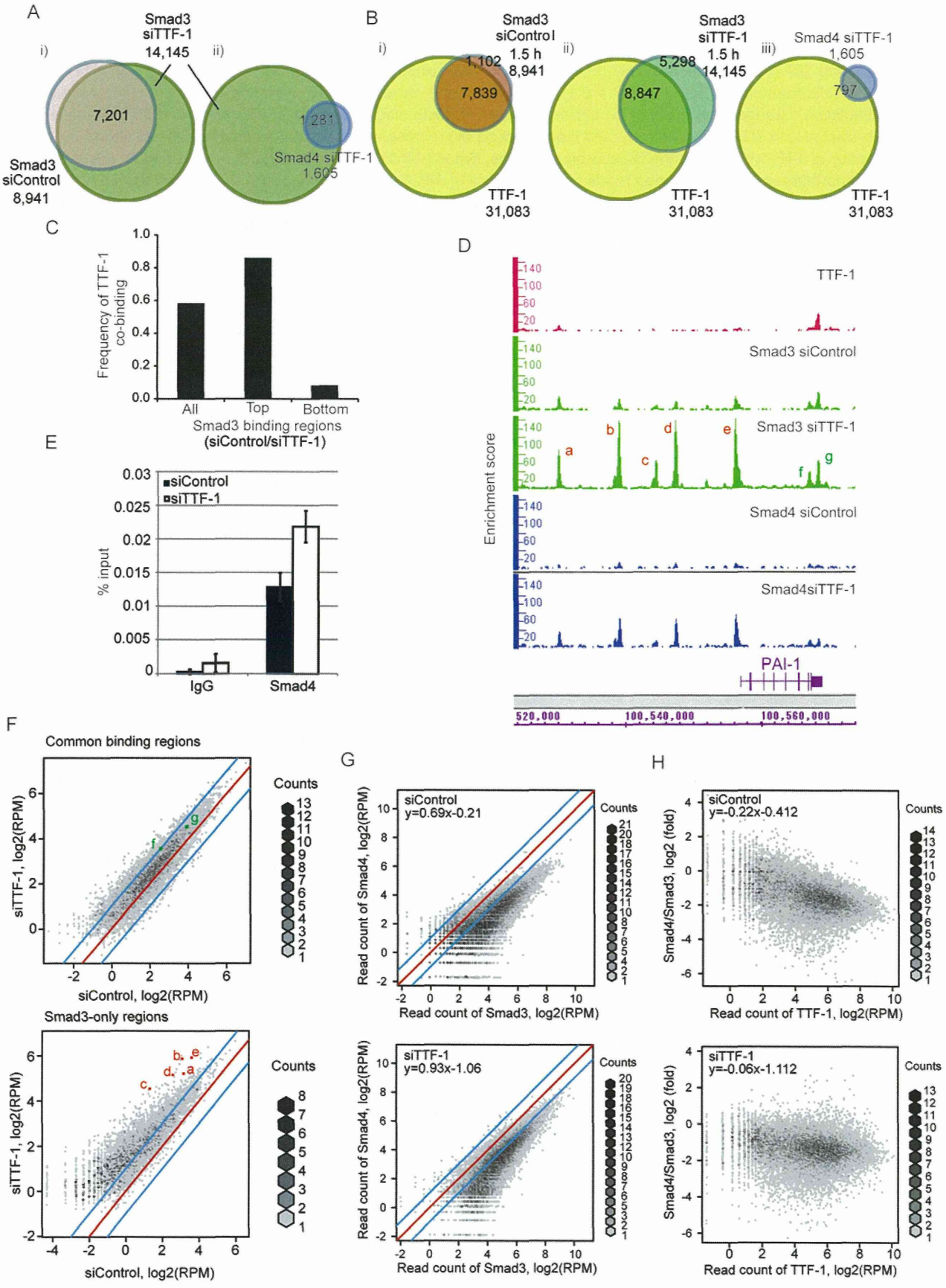
A
Smad3 siTTF-1 14,145
i)
ii)
7,201
1,281
Smad4 siTTF-1 1,605
Smad3 siControl 8,941
B
Smad3 siControl 1.5 h 8,941
Smad3 siTTF-1 1.5 h 14,145
Smad4 siTTF-1 1,605
1,102
7,839
5,298
8,847
797
TTF-1 31,083
C
Frequency of TTF-1 co-binding
All
Top
Bottom
Smad3 binding regions (siControl/siTTF-1)
D
TTF-1
Smad3 siControl
Smad3 siTTF-1
Smad4 siControl
Smad4siTTF-1
Enrichment score
PAI-1
E
siControl
siTTF-1
% input
IgG
Smad4
F
Common binding regions
siTTF-1, log2(RPM)
siControl, log2(RPM)
Counts
Smad3-only regions
G
siControl y=0.69x-0.21
Read count of Smad4, log2(RPM)
Read count of Smad3, log2(RPM)
siTTF-1 y=0.93x-1.06
H
siControl y=-0.22x-0.412
Smad4/Smad3, log2 (fold)
Read count of TTF-1, log2(RPM)
siTTF-1 y=-0.06x-1.112

Figure 2 ChIP-seq analysis reveals colocalization of Smad3 and TTF-1, and competition of Smad4 and TTF-1 on chromatin in H441 cells. **(A, B)** Comparison of the numbers of Smad3-, Smad4- and TTF-1-binding regions in H441 cells obtained from ChIP-seq analyses. **(A)** i: Pink and green circles represent Smad3-binding regions in H441 cells treated with TGF-β for 1.5 h with control and TTF-1 siRNA, respectively (FDR = 0.01). ii: Blue circle represents Smad4-binding regions in siTTF1-transfected H441 cells treated with TGF-β (FDR = 0.1). **(B)** Yellow circle represents TTF-1-binding regions in H441 cells without TGF-β stimulation. Orange (i) and green (ii) circles represent Smad3-binding regions in siControl- and siTTF-1-transfected H441 cells treated with TGF-β, respectively, and the blue circle (iii) represents the Smad4-binding regions as shown in **A**-ii. **(C)** The frequency of TTF-1-binding at the Smad3-binding sites. Smad3-binding strength at each binding region was defined as read counts normalized by total mapped reads of the dataset (14 145 Smad3-binding peaks determined in H441 cells transfected with siTTF-1). The read count ratio of each binding region was obtained by calculating the normalized read counts of siControl/siTTF-1. The frequency of Smad3-binding sites common to TTF-1 was calculated in two groups: the top 2 000 and bottom 2 011 regions with high and low siControl/siTTF-1 ratios, respectively. **(D)** TTF-1-, Smad3- and Smad4-binding regions in the *PAI-1* gene locus. Peaks a-e indicate Smad3-only regions; peaks f and g indicate Smad3-TTF-1 common regions. **(E)** ChIP-reChIP analysis of Smad3-Smad4 co-binding to DNA in H441 cells. Cells were stimulated with TGF-β for 1.5 h and fixed. Samples were eluted after anti-Smad3 ChIP, followed by secondary ChIP as indicated (IgG or anti-Smad4). Primers specific for the Smad3-binding region (peak e in Figure 2D) were used for evaluation by real-time PCR. **(F)** Read counts of Smad3-binding strength in the Smad3-TTF-1 common binding regions (upper panel) and the Smad3-only binding regions (lower panel) were obtained, and comparison was made in each region in TGF-β-treated H441 cells transfected with siControl and siTTF-1. Red dots (a-e) and green dots (f and g) indicate the binding regions shown in **D**. **(G)** Read counts in all Smad3-binding regions were obtained from the Smad3-ChIP-seq and Smad4-ChIP-seq data of TGF-β-treated H441 cells transfected with siControl (upper panel) or siTTF-1 (lower panel), and read counts of Smad3 and Smad4 were compared in each region. **(H)** Binding strengths of TTF-1 were determined as normalized read counts of TTF-1 and compared with the relative read counts' ratios of Smad4/Smad3 in the Smad3-binding sites in H441 cells transfected with siControl (upper panel) or siTTF-1 (lower panel). RPM, reads per million mapped reads.

increase more than two-fold in H441 cells with siTTF-1 compared with cells with siControl, while the read counts in the Smad3-only regions increased more than two-fold in the siTTF-1-treated cells. Taken together, these findings suggest that TTF-1 mainly inhibits Smad3 binding in Smad3-only regions.

Inhibitory effect of TTF-1 on the binding of Smad4 to chromatin

We obtained and analyzed read counts of Smad4 binding in all of the Smad3-binding regions of H441 cells with siTTF-1 from the Smad4 ChIP-seq data. Then, we compared the binding strengths of Smad3 and Smad4 in each Smad3-binding peak, and analyzed them by scatter plotting (Figure 2G). Regardless of the presence of siControl and siTTF-1, the binding strengths of Smad3 and Smad4 were strongly correlated. However, the slope of the regression curve was sharper for cells treated with siTTF-1 than for cells treated with siControl. Thus, the binding strength of Smad4 may be weaker in the presence of TTF-1 than in its absence, especially where strong binding peaks of Smad3 were observed.

As TTF-1 appeared to affect Smad4-chromatin binding more strongly than Smad3-chromatin binding, we obtained read counts of TTF-1 in the absence of TGF-β treatment in the Smad3-binding regions shown in Figure 2G (upper panel), and compared them with the relative binding strengths of Smad3 and Smad4 by calculating the read count ratios of Smad4/Smad3 (Figure 2H). Smad4/Smad3 read count ratios diminished in peaks where TTF-1 strongly bound to chromatin together with Smad3 in H441 cells treated with siControl. In contrast, there is no correlation between TTF-1-binding strengths and Smad4/Smad3 read count ratios observed in siTTF-1-treated cells. In such case Smad4 bound to chromatin equally well, regardless of whether the chromatin regions represent Smad3-TTF-1 common regions or Smad3-only regions (data not shown). Therefore, TTF-1 may compete with Smad4 to bind to Smad3.

TTF-1 suppresses the expression of EMT-related genes and regulates that of apoptosis-related genes

We obtained expression array data from H441 cells with siTTF-1 or siControl in the presence and absence TGF-β stimulation. The knockdown efficiency of TTF-1 by siRNA was confirmed (Supplementary information, Figure S4A). We chose 1 049 genes that were expressed in H441 cells and induced by TGF-β stimulation. We compared changes in mRNA expression levels of these genes and Smad3-binding signals in their promoter regions between cells transfected with siControl and siTTF-1, and found that elevation of Smad3-binding signals was correlated with the upregulation of gene expression in siTTF-transfected cells (Figure 3A). Representative genes, whose expression was induced by TGF-β and enhanced more than two-fold by knockdown of TTF-1, are shown in Supplementary information, Table S7.

We next performed ontology analysis of the microar-

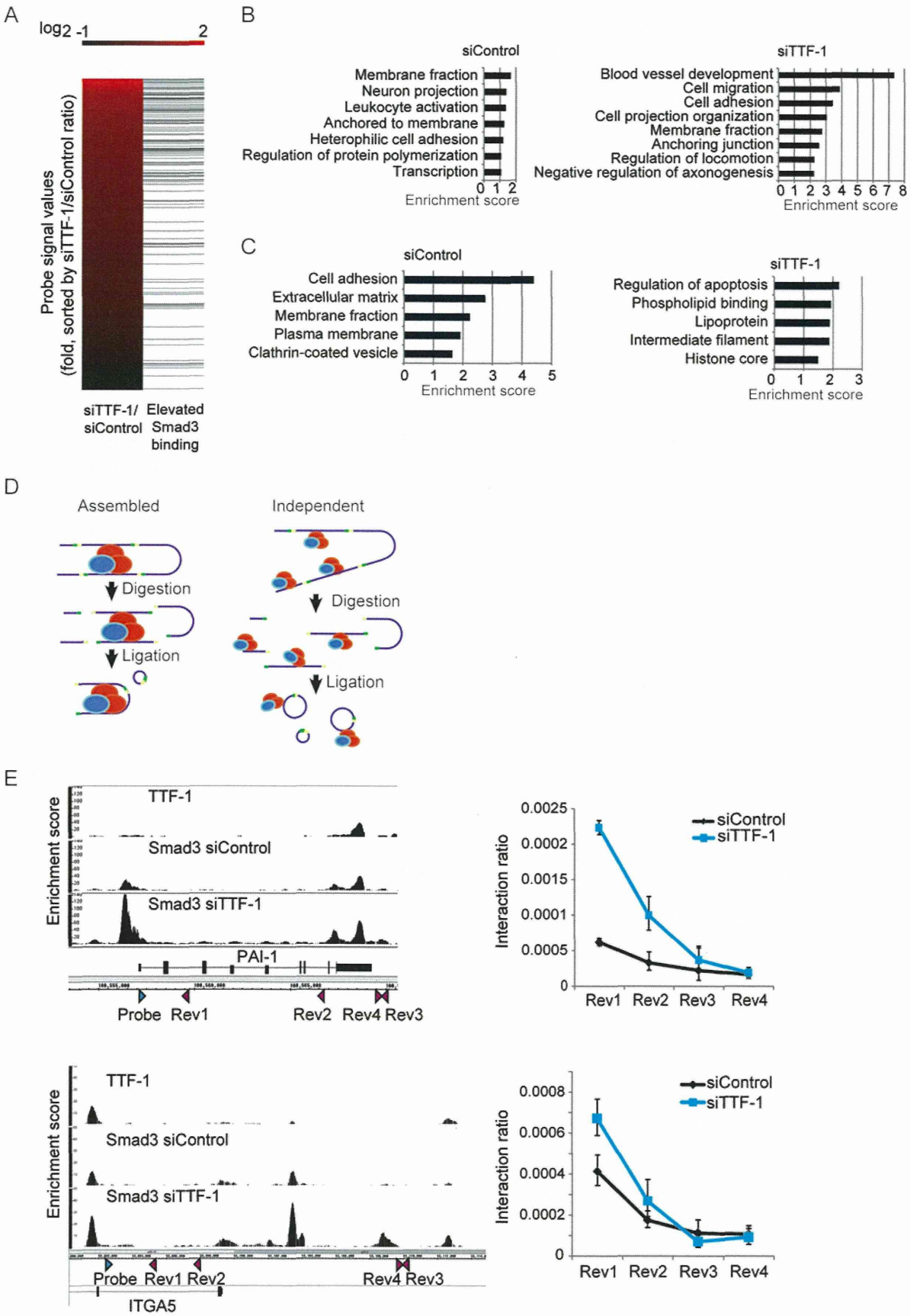
A
log2 -1
2
Probe signal values
(fold, sorted by siTTF-1/siControl ratio)
siTTF-1/ siControl
Elevated Smad3 binding
B
siControl
Membrane fraction
Neuron projection
Leukocyte activation
Anchored to membrane
Heterophilic cell adhesion
Regulation of protein polymerization
Transcription
0 1 2
Enrichment score
siTTF-1
Blood vessel development
Cell migration
Cell adhesion
Cell projection organization
Membrane fraction
Anchoring junction
Regulation of locomotion
Negative regulation of axonogenesis
0 1 2 3 4 5 6 7 8
Enrichment score
C
siControl
Cell adhesion
Extracellular matrix
Membrane fraction
Plasma membrane
Clathrin-coated vesicle
0 1 2 3 4 5
Enrichment score
siTTF-1
Regulation of apoptosis
Phospholipid binding
Lipoprotein
Intermediate filament
Histone core
0 1 2 3
Enrichment score
D
Assembled
Independent
Digestion
Ligation
Digestion
Ligation
E
Enrichment score
TTF-1
Smad3 siControl
Smad3 siTTF-1
PAI-1
Probe Rev1
Rev2 Rev4 Rev3
Interaction ratio
0.0025
0.0002
0.0015
0.0001
0.0005
0
siControl
siTTF-1
Rev1 Rev2 Rev3 Rev4
Enrichment score
TTF-1
Smad3 siControl
Smad3 siTTF-1
Probe Rev1 Rev2
Rev4 Rev3
ITGA5
Interaction ratio
0.0008
0.0006
0.0004
0.0002
0
siControl
siTTF-1
Rev1 Rev2 Rev3 Rev4

Figure 3 TTF-1 knockdown affects gene expression and genomic interactions at regions with multiple Smad3-binding sits. **(A)** Comparison of the microarray data of genes induced by TGF-β in H441 cells and ChIP-seq data of Smad3. Left column: data from the expression array. Genes expressed in H441 cells and induced by TGF-β stimulation are selected and arranged with respect to siTTF-1/siControl ratios (changes in gene expression levels between siTTF-1 and siControl cells). Right column: Smad3 ChIP-seq data. Black bars indicate Smad3 binding with two-fold upregulation by siTTF-1. **(B)** Gene ontology analysis of the expression microarray data of H441 cells transfected with siControl or siTTF-1. Effect of the knockdown of TTF-1 on TGF-β-induced changes in gene expression was evaluated by comparing the enriched gene ontology clusters (left vs right) obtained by DAVID. **(C)** Gene ontology analysis of the function of TTF-1 in the absence of TGF-β stimulation. Acquisition of gene ontology clusters was performed as in **B**. **(D)** The 3C assay. Left: if a Smad complex binds to multiple sites in the promoter and assembles different regions after DNA digestion, interaction between multiple binding sites can be detected. Right: if a Smad complex binds to a single site in the promoter and fails to assemble different regions after DNA digestion, interaction between multiple binding sites cannot be observed. **(E)** Left panels: designed 3C Taqman probes (blue triangles) and primers (orange triangles) in the *PAI-1* and *ITGA5* loci. We designed four primers (including one with the opposite direction). The scheme of the *PAI-1* promoter (upper left) is a modification of Figure 2D. Right panels: interaction ratios were normalized by input values. Rev1-Rev4 indicate the reverse primers shown in the left panels. Error bars = SD.

ray data using DAVID [30]. We chose genes whose expression levels were increased upon TGF-β stimulation in cells transfected with siControl or siTTF-1. Upon TGF-β stimulation, only small increases in enrichment scores were seen in the presence of TTF-1, while knockdown of TTF-1 increased expression of many genes, including cell migration- and locomotion-related genes, in addition to genes involved in blood vessel development (Figure 3B). Notably, induction of *SNAI1* and *SNAI2* by TGF-β was enhanced upon knockdown of TTF-1 (Supplementary information, Figure S4B and S4C). Some of the Smad3-binding peaks around these genes represented Smad3-only regions and the binding strengths of Smad3 were strongly affected by TTF-1 expression.

We also analyzed TTF-1-regulated genes in the absence of TGF-β by comparing gene expression in siControl and siTTF-1 cells. We chose genes whose expression levels were upregulated in cells transfected with siControl (Figure 3C, left) or siTTF-1 (Figure 3C, right) without TGF-β stimulation. We found that TTF-1 up-regulated cell adhesion-related genes, and that knockdown of TTF-1 enhanced expression of apoptosis-related genes. Taken together, these data suggest that TTF-1 suppresses TGF-β-induced EMT-related genes involved in cell migration and locomotion and protects cells from apoptosis in H441 cells.

Knockdown of TTF-1 enhances the interaction between multiple Smad3-binding regions in Smad3/Smad4 target genes

As shown in Figure 2D and Supplementary information, Figure S4B, we observed multiple Smad3-binding sites around a single target gene locus. Some represent Smad3-TTF-1 common regions, and others are Smad3-only regions. Therefore, it is possible that one Smad complex might bind to multiple sites through the MH1 domains of Smad3 and Smad4 or indirectly through other protein(s); alternatively, each Smad complex may bind to only one SBE. To test this, we performed a chromatin conformation capture (3C) assay. If each Smad protein in the Smad complex binds to the SBE independently and they act together to link distant genomic regions, we can detect interaction(s) of recognition sites of the restriction enzyme between multiple Smad-binding sites (Figure 3D, left). If each Smad complex can bind to only one SBE, such interactions cannot be observed (Figure 3D, right).

We designed probes and primers in two target gene regions, *PAI-1* and *ITGA5* (Figure 3E). In both regions, a probe was designed immediately downstream of one Smad3-binding site and primers were designed upstream and downstream of other Smad3-binding sites. One of the Smad3-binding sites is common to TTF-1 where Smad3 can bind to chromatin regardless of TTF-1 expression, and the other(s) is Smad3-only region(s) where Smad3-binding strength is weak in the presence of endogenous TTF-1. We detected enhanced interaction using primers upstream of the Smad3-binding sites in cells treated with siTTF-1, and minimal interaction was observed using primers downstream of the Smad3-binding regions. Taken together, these data suggest the existence of interactions between different SBEs in the promoters of *PAI-1* and *ITGA5* genes, which could be enhanced by TTF-1 knockdown.

Smad3 binds to certain DNA regions with TTF-1 in the absence of TGF-β stimulation and regulates target gene expression

Next, we analyzed Smad3-binding regions, which were identified only in cells with siControl but not with siTTF-1 (Figure 2A-i). These Smad3-binding peaks were common to TTF-1 binding, and were therefore

termed Smad3-TTF-1-requiring loci (STRL). We identified the genes nearest to these loci, and compared their expression in the presence and absence of TGF-β. Genes located near the STRL, whose expression levels were reduced by more than half after 24 h of TGF-β stimulation, are shown in Supplementary information, Table S8, including *LMO3*, which exhibits pro-survival effects in adenocarcinoma cells [14]. To determine whether Smad3 binding to the STRL is regulated by TGF-β signaling, we performed ChIP-qPCR analysis at these loci in the presence of TGF-β or the TGF-β type I receptor inhibitor SB431542. Surprisingly, Smad3 bound strongly to these loci in the presence of SB431542, and TGF-β treatment reduced the respective binding strengths of Smad3 to these loci (Figure 4A, left). Moreover, knockdown of Smad4 did not attenuate Smad3 binding to these loci (Figure 4A, right), suggesting that Smad3 binds to these loci independently of Smad4. We confirmed colocalization of Smad3 and TTF-1 at the *LMO3* region by sequential ChIP using TTF-1 and Smad3 antibodies (Supplementary information, Figure S5). We also found that Smad2 colocalized with TTF-1 at this region, possibly through interaction of Smad2 with Smad3. We examined whether Smad3 or Smad4 affects mRNA expression of these genes, and found that knockdown of either Smad3 or Smad4 cancelled the effects of TGF-β (Figure 4B). By knocking down Smad3, the basal expression level of LMO3 was increased, whereas those of SDPR and FBP1 were reduced, suggesting that Smad3 could act as both a repressor and an activator of genes close to the STRL. Expression levels of those genes in A549 cells (which lack endogenous TTF-1 expression) were comparable to those in H441 cells (which express TTF-1) treated with TGF-β for 24 h, suggesting that binding of TTF-1-Smad3 complex to these target regions is important for regulating the expression of these genes in H441 cells.

Finally, we performed Smad3 ChIP-seq analysis using A549 cells treated with TGF-β, and compared binding regions of Smad3 with those in H441 cells. Approximately 20% of the Smad3-binding regions were observed at STRL in H441 cells which express TTF-1, while only 1% of them were observed at STRL in A549 cells (Figure 4C). In A549 cells treated with TGF-β, Smad3 failed to bind to the STRL at *LMO3*, *SDPR* or *FBP1* (Supplementary information, Table S9). Read counts of Smad3 were obtained at the Smad3-binding regions in A549 cells treated with TGF-β (Supplementary information, Table S9), and compared to those in H441 cells treated with siTTF-1, using scatter plotting (Figure 4D, left). We have also obtained read counts of Smad3 in A549 cells at the STRL in H441 cells, and compared to those in H441 cells treated with siControl (Figure 4D, right). Correlation of the read counts in Smad3-binding regions was observed between A549 cells and H441 cells treated with siTTF-1 (correlation coefficient = 0.479), while no correlation was observed between A549 cells and H441 cells with siControl in terms of Smad3 binding to the STRL (Figure 4D). These findings suggest that certain portions of Smad3-binding regions in A549 cells are common to those in other lung adenocarcinoma cells, and that Smad3 binding to STRL requires the expression of TTF-1.

Discussion

Smad4-dependent and -independent functions of Smad3

We demonstrated that TTF-1 binds to Smad3 both in the presence and absence of TGF-β stimulation and its presence decreases the amount of Smad3-Smad4 complex in the nucleus (Figure 1A-1D). TTF-1 inhibits both Smad3 and Smad4 binding to chromatin, but in different ways. Smad3 colocalizes with TTF-1 in certain chromatin regions (Figure 2B), while Smad4 was not detected at chromatin in the presence of TTF-1 in the *PAI-1* regions (Figure 2D). In addition, Smad4-binding strengths were weaker than those of Smad3 at the Smad3-binding sites where TTF-1 strongly bound, and this tendency was cancelled by knockdown of TTF-1 (Figure 2H). These findings suggest that TTF-1 competes with Smad4 for interaction with Smad3 at the whole Smad-binding sites of the genome.

Our present findings also revealed that Smad3 binds to chromatin with TTF-1, but not with Smad4, in certain regions (Figure 5). Smad3 binds to the promoter regions of *SDPR* and *FBP1*, and the second intron of *LMO3*, where TTF-1 is also able to bind, in the absence of TGF-β signaling. TGF-β stimulation reduces the binding strengths of Smad3 at these sites, while knockdown of Smad4 enhanced or did not significantly affect them (Figure 4A). Thus, in cells expressing TTF-1, Smad3 binds to chromatin with TTF-1 without TGF-β stimulation, and the Smad3-TTF-1 complex regulates expression of different target genes from those regulated by the Smad3-Smad4 complex.

There are some reports that Smad3 regulates the expression of target genes in a Smad4-independent manner [31-34]. TRIM33 (also known as TIF1γ and ectodermin) competes with Smad4 for interaction with Smad3 upon TGF-β stimulation, and transduces signals independently of Smad4 through the TRIM33/Smad3 complex [33]. Also, SARS-associated coronavirus nucleocapsid protein was reported to interact with Smad3, acting competitively with Smad4, and modulate the expression of target genes of TGF-β signaling [34]. In contrast to these cases,

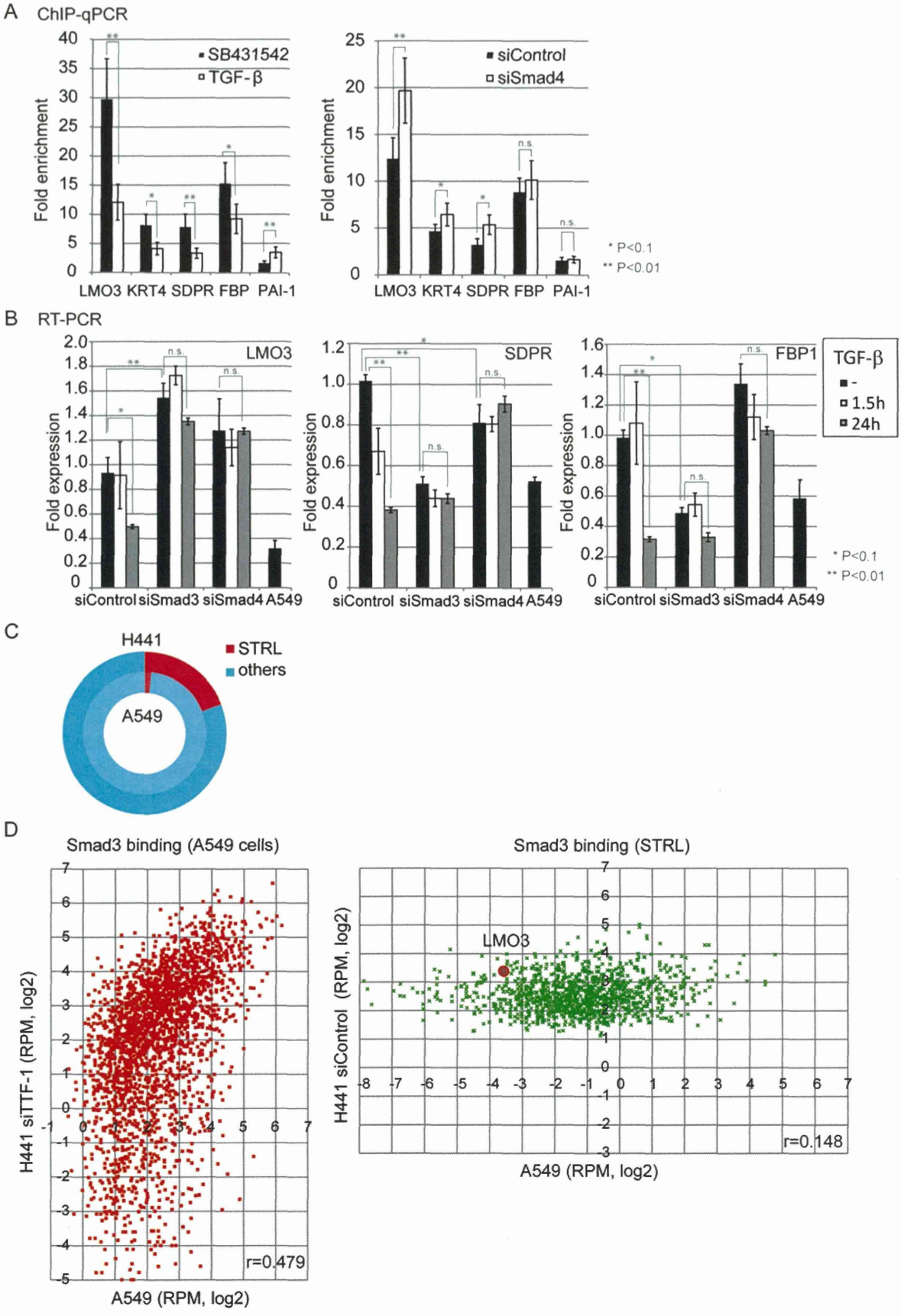
A
ChIP-qPCR
SB431542
TGF-β
Fold enrichment
LMO3 KRT4 SDPR FBP PAI-1
siControl
siSmad4
* P<0.1
** P<0.01
B
RT-PCR
LMO3
SDPR
FBP1
TGF-β
-
1.5h
24h
Fold expression
siControl siSmad3 siSmad4 A549
C
H441
STRL
others
A549
D
Smad3 binding (A549 cells)
H441 siTTF-1 (RPM, log2)
A549 (RPM, log2)
r=0.479
Smad3 binding (STRL)
LMO3
H441 siControl (RPM, log2)
r=0.148

Figure 4 Smad3 binds to certain chromatin regions with TTF-1 independently of Smad4 in the absence of TGF-β stimulation. **(A)** Left: H441 cells were treated with SB431542 or TGF-β for 1.5 h. ChIP-qPCR was performed using Smad3 antibody. Right: H441 cells were treated with control or Smad4 siRNAs for 48 h without TGF-β stimulation, and ChIP-qPCR was performed using Smad3 antibody. LMO3, LIM-domain only-3; KRT4, keratin 4; SDPR, serum deprivation response; and FBP, fructose-1,6-biphosphatase. **(B)** mRNA expression of target genes near the STRL. H441 cells were treated with control, Smad3, or Smad4 siRNAs for 48 h, and A549 cells were treated with control siRNA for 48 h. H441 cells were stimulated with TGF-β as indicated. RT-PCR analyses were performed using primers specific for LMO3 (left), SDPR (middle) or FBP1 (right). **(C)** Comparison of Smad3-binding loci between A549 cells (inner circle) and H441 cells treated with siControl (outer circle). Red parts show loci which are observed at STRL. **(D)** Read counts of Smad3 at the Smad3-binding regions in A549 cells were obtained, and comparison was made in each region between A549 cells and H441 cells transfected with siTTF1 (left panel). Read counts of Smad3 at the STRL of H441 cells were also obtained from A549 cells and from H441 cells treated with siControl, and comparison was made in each region (right panel). *r*, Pearson's correlation coefficient; RPM, reads per million mapped reads.

TTF-1 forms complexes with Smad3 without TGF-β stimulation. Thus, the Smad4-independent function of Smad3 demonstrated in the present study differs from that induced by the other reported factors.

Mutual inhibition between TGF-β and TTF-1 signaling

The effects of TTF-1 on tumor progression appear to be context dependent [35]. TTF-1 exhibits pro-survival effects through induction of ROR1 and/or LMO3 [13, 14]. In the present study, we have shown that LMO3 expression was regulated by the Smad3-TTF-1 complex in H441 cells. On the other hand, TTF-1 inhibits TGF-β-induced EMT [28], and thus functions as a tumor suppressor gene. TTF-1 may thus have two different effects that are opposite to the effects induced by TGF-β signaling: pro-survival and anti-EMT functions. The ontology analysis of the microarray data of H441 cells by DAVID (Figure 3B and 3C) supports these observations.

TTF-1 regulates specific genes in alveolar epithelial cells, while TGF-β induces EMT. Thus, the balance between TTF-1 expression and TGF-β signaling may be very important for differentiation of lung epithelial cells and progression of lung adenocarcinoma. TTF-1 inhibits parts of TGF-β signaling, and TGF-β conversely inhibits the function of TTF-1. Interaction of Smad3 with TTF-1 did not alter the binding profiles of TTF-1 to chromatin (Supplementary information, Figure S6A and S6B). Of note, TGF-β reduced the expression of TTF-1 mRNA only at later time points (Supplementary information, Figure S4A), while TTF-1 binding to chromatin was rapidly inhibited by TGF-β, suggesting that some other mechanisms are important in regulation of the function of TTF-1 by TGF-β signaling.

We previously reported that TTF-1 inhibits TGF-β-induced EMT, and suggested that inhibition of the expression of Snail and/or Slug by TTF-1 is important. We also detected up-regulation of *SNAI1* and *SNAI2* expression levels (encoding Snail and Slug, respectively) in H441 cells by TGF-β (Supplementary information, Figure S4B and S4C). Furthermore, we observed that expression levels of some other genes that are known to be involved in EMT are regulated by TGF-β and TTF-1. *ITGA5* is reportedly up-regulated during EMT. Moreover, integrin α5 (encoded by *ITGA5*) interacts with the extracellular matrix and enhances cell migration [36]. Using the 3C assay, we observed enhanced Smad3 binding to the *ITGA5* promoter and the interaction of distant chromatin regions around the ranscription start site in H441 cells upon TTF-1 knockdown. Thus, *ITGA5* might be another direct target of TGF-β, which is suppressed by TTF-1. Also, some genes shown in Supplementary information, Table S7, e.g., *LOX* and *RUNX2*, have been reported to promote EMT in some carcinomas [37, 38]. These genes may play important roles in the progression of malignancy.

Cellular context-dependent function of the TTF-1-Smad3 complex

In the present study, we have shown that the TTF-1-Smad3 complex regulates the expression of genes different from those regulated by the canonical TGF-β-Smad pathway. In H441 cells, knockdown of TTF-1 enhanced the expression of pro-apoptotic genes in the absence of TGF-β stimulation as well as the induction of EMT-related genes upon TGF-β stimulation. TTF-1 inhibits apoptosis of lung epithelial cells, and the TTF-1-Smad3 complex may modulate the expression of apoptosis-related genes. *LMO3* is one of such genes regulated by the TTF-1-Smad3 complex, though Smad3 has a suppressive effect on its expression (Figure 4B).

We also obtained RNA-seq data using TTF-1-deficient A549 cells, and performed ontology analysis (Supplementary information, Figure S7A), as in H441 cells (Figure 3B and 3C). Ectopic expression of TTF-1 inhibited the expression of cell motion-related genes induced by TGF-β, but did not enhance that of pro-survival-related

genes, including *LMO3* (Supplementary information, Figure S7A). One of the reasons that ectopic TTF-1 failed to upregulate some of its target genes in A549 cells might be due to epigenetic changes. Based on a public database (GEO accession no. GSM999365), CpG methylation was present in the *LMO3* locus in A549 cells (data not shown). Moreover, cell growth assay revealed that TTF-1 inhibits the proliferation of A549 cells (Supplementary information, Figure S7B), suggesting that the function of TTF-1 in cell proliferation and apoptosis varies according to cellular contexts, although inhibitory effects of TTF-1 on the Smad3-Smad4 complex and EMT are maintained.

Tissue-specific expression of transcription factors and modification of Smad3 binding

We propose a hypothesis that each Smad protein in the Smad complex binds to distinct Smad-binding sites, resulting in an assembly connecting multiple promoter and/or enhancer regions of a target gene (Figure 5). Smad3 and Smad4 may also bind to chromatin indirectly through other proteins. Thus, the increased interaction of promoter and enhancer regions demonstrated in the 3C assay may reflect enhanced binding between Smads and other transcription factors.

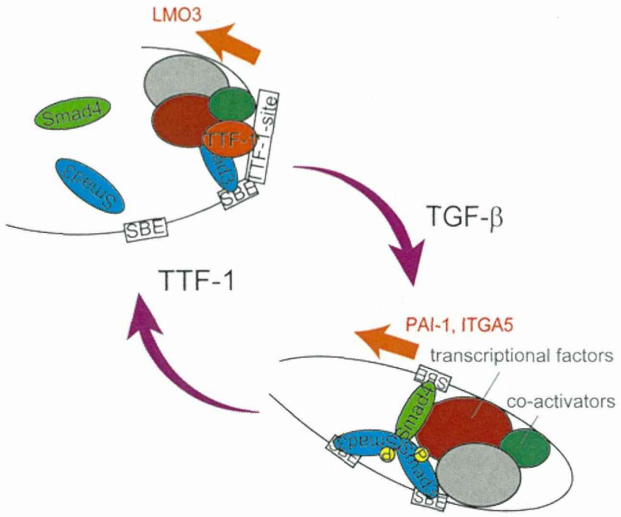

Figure 5 Smad4-independent roles of Smad3 regulated by TTF-1. Scheme of Smad4-dependent and -independent functions of Smad3 in lung adenocarcinoma cells. The Smad3-Smad4 complex interacts with other transcription factors and transcriptional co-activators (or co-repressors), and regulates transcription of certain target genes, including *PAI-1* and *ITGA5*, leading to induction of EMT and other effects upon TGF-β stimulation. In the presence of TTF-1, the Smad3-Smad4 complex is disrupted, and TTF-1 interacts with Smad3 and other transcription factors and regulates certain other genes, including *LMO3*, leading to induction of cell survival and certain other effects in a cellular context-dependent manner.

Recent studies indicate that co-localization of cell-type-specific transcription factors and Smad3 is important for context-dependent outputs of TGF-β signaling [19, 21]. We have shown here that TTF-1, a lung epithelial-specific transcription factor, co-occupies with Smad3 on chromatin, and that loss of TTF-1 function greatly alters the binding profiles of Smad3, especially in regions where TTF-1 does not bind to chromatin. These tissue-specific factors seem not only to enable Smad3 to bind to specific regions, but also to inhibit Smad3 binding to certain regions. These factors may bind to unphosphorylated Smad3, as well as to the Smad3-Smad4 complex. Understanding the underlying regulatory mechanisms may help to elucidate the differences in progression and therapeutic response of cancers from different organs.

Materials and Methods

Cell culture

A549 cells were maintained in Dulbecco's modified Eagle's medium (#11965; Life Technologies) supplemented with 10% fetal bovine serum (FBS), 100 U/ml penicillin G and 100 μg/ml streptomycin. H441 cells were maintained in RPMI 1640 (#11875; Life Technologies) supplemented with 10% FBS, 100 U/ml penicillin G and 100 μg/ml streptomycin. Cells were grown in a humidified atmosphere with 5% CO_2 at 37 °C.

Reagents and antibodies

Recombinant TGF-β (TGF-β3) and the TGF-β type I receptor inhibitor SB431542 were purchased from R&D systems and Sigma-Aldrich (S4317), respectively. The following antibodies were used: mouse anti-FLAG (M2; Sigma-Aldrich), mouse anti-myc (9E10; Oncogene research products), rabbit anti-pSmad3 (C25A9; Cell Signaling), mouse anti-tubulin (DM1A; Sigma-Aldrich), rabbit anti-HDAC1 (2E10; Millipore), mouse anti-Smad2/3 (BD), rabbit anti-Smad3 (ab28379 and ab40854; Abcam), mouse anti-Smad4 (B-8; Santa Cruz), goat anti-Smad4 (AF2097; R&D) and mouse anti-TTF-1 (8G7G3/1; Novus Biologicals).

Immunoprecipitation and immunoblotting

Lysis buffer (1% NP-40, 150 mM NaCl, 50 mM Tris-HCl (pH 8.0), 5 mM EDTA, 1 mM phenylmethylsulfonyl fluoride and 10 μg/ml aprotinin) was used for cell lysis. Immunoprecipitation was performed as previously described [39]. Sodium dodecyl sulfate gel electrophoresis and immunoblotting were performed as described [39], using a SEPROS SV (Fujifilm, Japan) or a LAS-4000 lumino-image analyzer (Fujifilm, Japan).

Fractionation of the nucleus and cytoplasm

We used the NE-PER Nuclear and Cytoplasmic Extraction Kit (Thermo Scientific) according to the manufacturer's instructions.